Orbital mapping of energy bands and the truncated spin polarization in three-dimensional Rashba semiconductors

Qihang Liu,[1,*] Xiuwen Zhang,[1] J. A. Waugh,[2] D. S. Dessau,[1,2] and Alex Zunger[1]
[1]*University of Colorado, Boulder, Renewable and Sustainable Energy Institute, Boulder, Colorado 80309, USA*
[2]*Department of Physics, University of Colorado, Boulder, Colorado 80309, USA*
(Received 28 January 2016; revised manuscript received 1 September 2016; published 27 September 2016)

Associated with spin-orbit coupling (SOC) and inversion symmetry breaking, Rashba spin polarization opens an avenue for spintronic applications that was previously limited to ordinary magnets. However, spin-polarization effects in actual Rashba systems are far more complicated than what conventional single-orbital models would suggest. By studying via density functional theory and a multiorbital $k \cdot p$ model a three-dimensional bulk Rashba system (free of complications by surface effects), BiTeI, we find that the physical origin of the leading spin-polarization effects is SOC-induced hybridization between spin and multiple orbitals, especially those with nonzero orbital angular momenta. In this framework we establish a general understanding of the orbital mapping, common to the surface of topological insulators and the Rashba system. Consequently, the intrinsic mechanism of various spin-polarization effects—which pertain to all Rashba systems, even those with global inversion symmetry—is understood as a manifestation of the orbital textures. This finding suggests a route for designing high-spin-polarization materials by considering the atomic-orbital content.

DOI: 10.1103/PhysRevB.94.125207

I. INTRODUCTION

The coupling between the motion of electrons and spins leading to spin polarization without external magnetic field is the focus of the emerging field of spin-orbitronics [1,2], a branch of spintronics [3] that encompasses many interesting areas such as the Dresselhaus [4] and the Rashba [5] effects, spin-orbital torque [6,7], topological insulation [8], and Majorana fermions [9]. The idea of control of spin degree of freedom even without external magnetic field is based on the fact that in a non-centrosymmetric system, spin-orbit coupling (SOC) sets up an effective internal magnetic field that creates spin splitting $E_1(\boldsymbol{k}, \uparrow) - E_2(\boldsymbol{k}, \downarrow)$ between spin-up and spin-down components in bands 1 and 2 away from the time-reversal invariant wave vector K^*. Specifically, Rashba spin splitting provides a classical scenario of spin topology encoded already in a simplified *single-orbital* (e.g., one s band) Hamiltonian $H = \frac{\hbar^2 \boldsymbol{k}^2}{2m^*} + \lambda(\nabla V \times \boldsymbol{k}) \cdot \boldsymbol{\sigma}$, where fully spin-polarized bands form two oppositely rotating spin loops at the Fermi surface. However, the limitation of the single-orbital model is already acknowledged in areas of condensed matter physics, such as strongly correlated systems [10]. In real materials with spin coupling to *multiple* orbitals that make up the band eigenstates, the leading SOC spin effects that deviate from the classical single-orbital picture include the following: (i) The spin polarization $S_n(\boldsymbol{k})$ of each spin-split band $(n, \boldsymbol{k})$ appears to be truncated below its maximum value 100%. (ii) Each branch of the pair of spin-split bands (that are degenerate without SOC) experiences a different degree of spin truncation away from K^*, resulting in a net *spin polarization* for the band pair. (iii) The Rashba bands with two loops of energy contours can have identical helicities of spin texture. These effects were studied primarily in two-dimensional (2D) metallic surfaces - the classic Rashba systems [11–17]. Effects (i) and (ii) were theoretically discussed for freestanding Au(111) films [11], and in $BiAg_2$ metallic surface alloys [12,17], while effect (iii) was predicted in the unoccupied bands of Bi/Cu(111) [13] and Bi/Ag(111) [15] surface alloys. The physics behind these intriguing spin effects was briefly touched upon in the context of 2D Rashba metallic films as being a consequence of the coupling between spin and different in-plane orbitals [13,17]. However, in all 2D Rashba platforms noted above there is a need for a free surface to observe the effects, so ordinary surface effects (such as broken bonds and surface band bending [18]) can cloud the intrinsic mechanism of these spin effects to be well established [14].

By extending the spin effects (i–iii) from the originally studied 2D metallic Rashba systems to 3D surface-free bulk Rashba semiconductors, we provide two pertinent generalizations: (a) We use the construct of *orbital texture* [a k-space map $I_n^{(l,m)}(k_x, k_y)$ of the content of orbital m_l in band n; see Eq. (1)] familiar from topological insulators [19–23]. We point out that the effect of switch in orbital texture between two bands is common to topological insulators and to 3D Rashba semiconductors. Specifically, in the topologically trivial bulk Rashba semiconductor the orbital textures of different Rashba bands switch from "radial" to "tangential" (with respect to the energy contour) character at the band crossing wave vector K^*, in full analogy with the phenomena previously observed [20,23,24] and calculated [22,23] at the *surfaces* of 3D topological insulator (TI) Bi_2Se_3. Thus the switch of orbital texture and indeed effects (i–iii) are not specific to topological or Rashba effects, but originate fundamentally from the fact that energy bands in complex solids invariably show a mixture of different azimuthal total orbital angular momentum (OAM) m_j, and that SOC can induce hybridization specifically between spin and *multiple* orbitals, respectively. (b) We show that the spin polarization truncated by multiple orbital hybridization can be generalized even to systems with global inversion symmetry, manifesting the "hidden spin-polarization effect" [25]. The understanding of effects

*qihang.liu85@gmail.com

(i–iii) and their reflection in the switch in orbital texture could provide better design guidelines for material selection and for spin manipulation in actual material application, e.g., electron confinement induced by spin-flip backscattering [17] and spin-galvanic effect [26,27].

We reached these conclusions by applying density functional theory (DFT) and a multiband $k\cdot p$ model to a 3D bulk Rashba compound BiTeI [28]. We find that within the six energy bands near the Fermi level (E_F) there are (i) a large spin truncation per band at a certain K^* with the residual spin polarization ranging from 0% to 85%, far greater than the ∼5% seen in the Au [111] surface [11]; (ii) a net *spin polarization of band pairs* up to 50% for the top two valence bands, and (iii) identical spin-rotating loops at the occupied bands that can be examined by future angle-resolved photon emission spectroscopy (ARPES) measurements.

II. METHODS

We use DFT with the projector-augmented wave (PAW) pseudopotential [29] and the exchange correlation described by the generalized gradient approximation of Perdew, Burke and Ernzerhof (PBE) [30]. The energy cut off of the plane-wave basis is set to 500 eV, and the total energy minimization was performed with a tolerance of 10^{-5} eV. Spin-orbit coupling is calculated by a perturbation $\sum_{i,l,m} V_l^{\mathrm{SO}} \vec{L}\cdot\vec{S}|l,m,i\rangle\langle l,m,i|$ to the pseudopotential [31], where $|l,m,i\rangle$ is the angular momentum eigenstate of the ith atomic site. The orbital intensity and orbital-dependent spin polarization is calculated by projecting the wave functions $\psi_n(\boldsymbol{k})$ with plane-wave expansion on the orbital basis (spherical harmonics) of each atomic site, as written in the following:

$$\text{Orbital intensity}: \quad I_n^{(i,l,m)}(\boldsymbol{k}) = \langle\psi_n(\boldsymbol{k})|(|l,m,i\rangle\langle l,m,i|)|\psi_n(\boldsymbol{k})\rangle, \tag{1}$$

$$\text{Orbital-dependent spin polarization}: \quad S_n^{(i,l,m)}(\boldsymbol{k}) = \langle\psi_n(\boldsymbol{k})|(\boldsymbol{\sigma}\otimes|l,m,i\rangle\langle l,m,i|)|\psi_n(\boldsymbol{k})\rangle, \tag{2}$$

where n, $\boldsymbol{k}$, and $\boldsymbol{\sigma}$ denote band index, momentum, and the Pauli matrix, respectively. Note that in this study we only distinguish different $|l,m\rangle$ states by adding up all the sites. All these features are implemented in the Vienna *ab initio* package (VASP) [32].

III. TRUNCATED SPIN POLARIZATION, NET SPIN POLARIZATION, AND SPIN TEXTURE IN BiTeI

This compound is a 3D bulk semiconductor [space group $P3m1$; see Fig. 1(a)] that manifests strong SOC, the ensuing orbital hybridization, and a polar field due to the positively charged Bi-Te layer that connects to the negatively charged iodine layer. The consequent Rashba spin-split bands [28,33] from DFT calculations are shown in Fig. 1(b). We focus on the top four hole bands VB1–VB4 (going down from E_F) and the bottom two electron bands CB1and CB2 (going up from E_F) around the $K^* = A(0,0,0.5)$ wave vector. The spin polarization $S_n(\boldsymbol{k})(n = \text{VB1–VB4, CB1, CB2})$ along the k_y direction is shown in Fig. 1(c). In what follows we discuss spin effects (i–iii) in bulk BiTeI:

(i) *Truncation of single-band spin polarization.* The band-by-band spin polarization is calculated as the expectation value of the spin operator in each of the six spin-split bands at the wave vector K^*. We find that the magnitude of spin polarization is below the maximal magnitude of 100%. For VB1, VB2 and CB1, CB2 the spin polarization is ±85% and ±51%, respectively, while for VB3, VB4 the spin polarization is 0, i.e., a complete quenching of spin. Away from the band crossing wave vector K^* the spin polarization of VB1 and VB2 evolves quite differently with k_y. VB1 is highly spin polarized in the considered momentum range up to $S_{\mathrm{VB1}} = -96\%$, while VB2 loses its spin polarization rapidly with increasing k_y down to $S_{\mathrm{VB2}} = 46\%$.

(ii) *Net spin polarization of pairs of spin-split bands.* If we sum $S_{\mathrm{VB1}}(\boldsymbol{k})$ and $S_{\mathrm{VB2}}(\boldsymbol{k})$ (which would add up to zero in the absence of SOC), we find a *net* spin up of −50% at $k_y = 0.06\,\text{Å}^{-1}$. On the other hand, the sum of $S_{\mathrm{VB3}}(\boldsymbol{k})$ and $S_{\mathrm{VB4}}(\boldsymbol{k})$ reaches 48% at $k = 0.06\,\text{Å}^{-1}$, while $S_{\mathrm{CB1}}(\boldsymbol{k})$ and $S_{\mathrm{CB2}}(\boldsymbol{k})$ change slightly with k. We note that the position of the net polarization peak does not overlap with the energy peak in the band structure which locates at $k = 0.09\,\text{Å}^{-1}$ in the k_y direction, suggesting that the spin polarization is not a reflection of the eigenvalue dispersion.

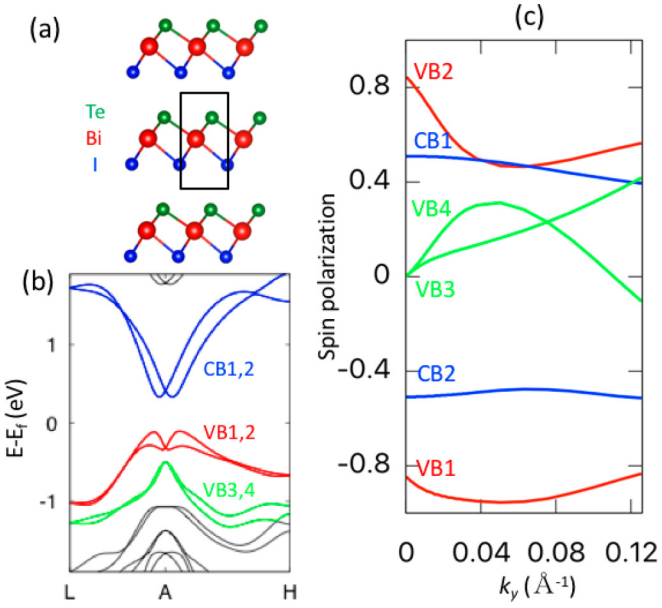

FIG. 1. (a) Crystal structure and (b) DFT band structure of BiTeI along the high-symmetric line L(0,0.5,0.5), A(0,0,0.5), H(1/3,1/3,0.5). (c) Spin polarization $S_n(\boldsymbol{k})$ of the six bands VB1–VB4 and CB1 and CB2 along the k_y direction at the $k_x = 0$ cut. Note that spin polarization at $k_y < 0$ fulfills $S_1(-\boldsymbol{k}) = -S_2(\boldsymbol{k})$ due to Kramer's degeneracy.

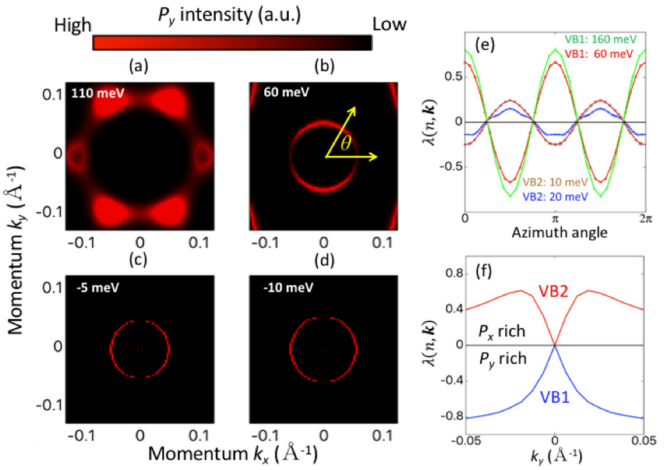

FIG. 2. (a–d) Orbital texture indicated by p_y intensity at different energy contours relative to the band crossing point: (a,b) for VB1 and (c,d) for VB2. (e,f) In-plane orbital polarization λ for (a) different energy contours as a function of the azimuth angle θ defined in panel (b), and for (f) different spin-splitting bands as a function of the momentum k_y at the $k_x = 0$ cut. Note that the orbital polarization switches signs exactly at the band crossing point $k_y = 0$.

(iii) *Identical directions of spin rotation in the helical spin texture bands.* The band pair VB1+VB2 and the pair CB1+CB2 show the classical Rashba-type spin texture, i.e., opposite helicities of spin loops. However, as shown in Fig. 1(c) before S_{VB4} falls below 0, S_{VB3} and S_{VB4} have the same sign, implying two spin loops with the same helicity in the area of $|k_{//}| < 0.10\,\text{Å}^{-1}$.

All three spin effects discussed above are absent in the conventional single-orbital model and thus reflect a manner of the complex interplay between spin and various OAM under the regime of SOC. To get a full picture it is useful to consider the *orbital texture*, i.e., the k-space map $I_n^{(l,m)}(k_x,k_y)$ of the content of orbital m_l in band n.

IV. ORBITAL TEXTURE AND ITS BEHAVIOR FOR DIFFERENT BANDS

In real solids the orbital content generally varies with the wave vector and band index, reflecting the changing symmetry. The orbital intensity is obtained by projecting the SOC-relevant band eigenstate $(n, \boldsymbol{k})$ onto local orbitals on atomic sites as shown in Eq. (1). Figures 2(a)–2(d) show the DFT calculated orbital texture given by the p_y orbital intensity at different energy contours relative to K^*, for VB1 and VB2. We find that for VB1 the calculated p_y orbital texture component is maximal along the k_y direction and minimal along k_x (where the p_x orbital dominates the in-plane states). On the other hand, for VB2 the p_y orbital texture component is minimal along k_y and maximal along k_x. Thus the orbital textures of VB1 and VB2 are different from each other and dominated by *radial* and *tangential* in-plane orbital patterns, respectively. This difference leads to a radial-tangential orbital texture *switch.* To trace the switch between these two bands we follow Ref. [23] to define the in-plane orbital polarization λ as a function of momentum k and band index n as $\lambda(n,\boldsymbol{k}) = \frac{I(p_x)-I(p_y)}{I(p_x)+I(p_y)}$, where $I(p_{x,y})$ denotes the calculated orbital intensity of $p_{x,y}$. Figure 2(e) shows λ as a function of the in-plane azimuth angle θ [defined in Fig. 2(b)], confirming the switch of the intensity distribution in going from VB1 to VB2. Moreover, the intensity variation fits very well to a $\sin 2\theta$ or $\cos 2\theta$ distribution, with a period of π. As shown in Fig. 2(f), λ changes the sign as the momentum k_y, passing through K^*, indicating that the radial-tangential switch happens exactly at the band crossing wave vector. For VB3 and VB4 the orbital textures also have a switch between tangential and radial characters at K^* [see Figs. 3(a) and 3(b)]. On the other hand, in CB1 and CB2 both Bi and Te atoms have considerable $p_{x,y}$ components, but with different orbital textures. For $p_{x,y}$ orbitals of Bi atom there is a radial-tangential switch from CB1 to CB2, while for $p_{x,y}$ orbitals of Te atom the orbital switch has an opposite trend, i.e., tangential-radial [see Figs. 3(c)–3(f)]. This observation agrees closely with the recent ARPES measurement by King *et al.* on the conduction surface state of BiTeI [34], and further confirms that such intriguing behavior comes from the intrinsic bulk state rather than any surface effects.

V. UNIVERSALITY OF ORBITAL TEXTURE IN BULK RASHBA AND SURFACE OF Ti REVEALED BY $k \cdot p$ MODELING

The orbital texture switch between two bands at K^* in the topologically trivial semiconductor bears an interesting analogy to the recently observed ARPES measurements [20,23] and DFT calculations [22] at the *surfaces* of TI Bi_2Se_3. Here we use a multiorbital $k \cdot p$ model to illustrate how mixing orbitals of different m_l and m_j couple with spin and lead to the orbital texture switch and the spin-polarization effects (i–iii). The crucial basis set represented in terms of m_j is obtained in DFT; we now explicitly isolate it from all other DFT bands in the $k \cdot p$ model below. Taking VB1 and VB2 as an example, we consider the SOC Hamiltonian as a perturbative form, $H_R = \alpha(\sigma_y k_x - \sigma_x k_y)$, that is valid for both Rashba bulk and TI surface [22], and thus write the wave functions in the vicinity of K^* as

$$|\text{VB1},k\rangle = \frac{1}{\sqrt{2}}\left(\sqrt{1-\omega_{\text{VB}}^2} + \mu_{\text{VB}}k\right)|p_t\rangle \otimes |\text{LH}\rangle + \left[\frac{i}{\sqrt{2}}\left(-\sqrt{1-\omega_{\text{VB}}^2} + \upsilon_{\text{VB}}k\right)|p_r\rangle + (\omega_{\text{VB}} - \xi_{\text{VB}}k)|Z\rangle\right] \otimes |\text{RH}\rangle, \quad (3)$$

$$|\text{VB2},k\rangle = \frac{1}{\sqrt{2}}\left(-\sqrt{1-\omega_{\text{VB}}^2} + \mu_{\text{VB}}k\right)|p_t\rangle \otimes |\text{RH}\rangle + \left[\frac{i}{\sqrt{2}}\left(\sqrt{1-\omega_{\text{VB}}^2} + \upsilon_{\text{VB}}k\right)|p_r\rangle + (\omega_{\text{VB}} + \xi_{\text{VB}}k)|Z\rangle\right] \otimes |\text{LH}\rangle, \quad (4)$$

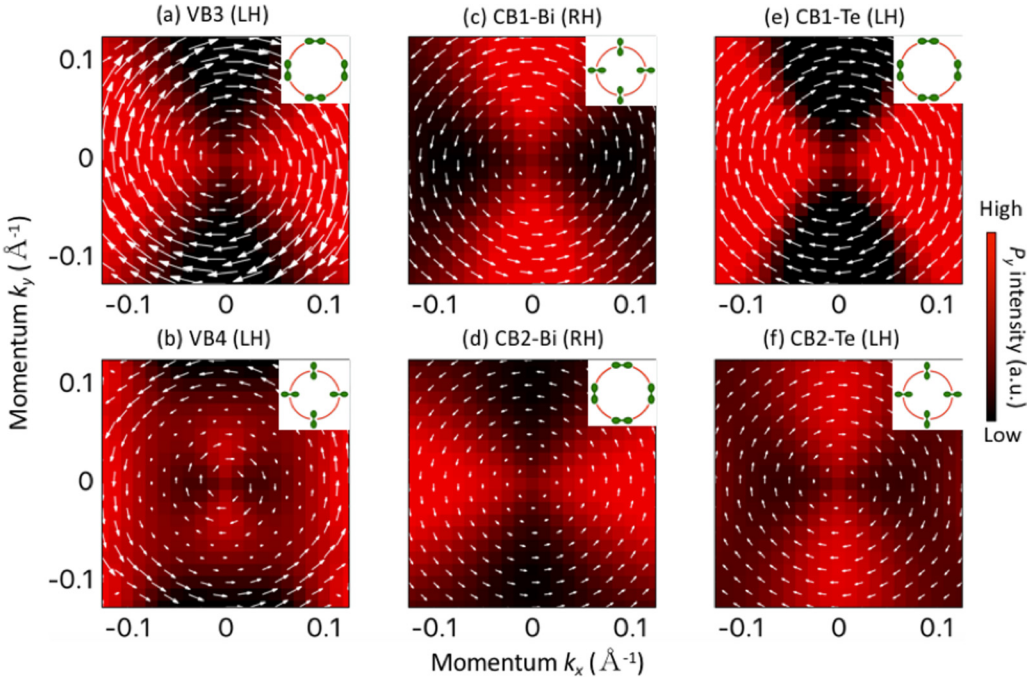

FIG. 3. (a,b) The in-plane p-dependent spin textures (white arrows) and orbital texture (denoted by p_y orbital intensity as background colors and the inset on the top right) of VB3 (a) and VB4 (b) in the vicinity of the band crossing point. (c,d) The in-plane Bi-p-dependent spin textures and orbital texture of CB1 (c) and CB2 (d) in the vicinity of the band crossing point. (e,f) Same as (c,d) but for Te-p-dependent spin textures of CB1 (e) and CB2 (f).

where the in-plane p orbital bases are tangential, $|p_t\rangle = -\sin\theta|p_x\rangle + \cos\theta|p_y\rangle$, and radial, $|p_r\rangle = \cos\theta|p_x\rangle + \sin\theta|p_y\rangle$; $|Z\rangle = \omega_s|s\rangle + \omega_z|p_z\rangle$ with $|\omega_s|^2 + |\omega_z|^2 = 1$; the spin bases are eigenstates of H_R; i.e., LH and RH helical spin states $|\mathrm{LH}\rangle = \frac{1}{\sqrt{2}}\begin{pmatrix} ie^{-i\theta} \\ 1 \end{pmatrix}$ and $|\mathrm{RH}\rangle = \frac{1}{\sqrt{2}}\begin{pmatrix} -ie^{-i\theta} \\ 1 \end{pmatrix}$; and ω_{VB}, υ_{VB}, ξ_{VB} are the wave-function coefficients that are band dependent. More details on these wave functions can be found in the Appendix. By calculating the difference of p_t and p_r intensity and omitting the higher-order k term we find that

$$[I(p_t) - I(p_r)]|_{\mathrm{VB1(VB2)}} = \pm|k|\left[\sqrt{1-\omega_{\mathrm{VB}}^2}(\mu_{\mathrm{VB}}^* - \upsilon_{\mathrm{VB}}^*) + \mathrm{c.c.}\right]. \quad (5)$$

From the modeling wave functions, Eqs. (3) and (4), and the difference of p_t and p_r intensity shown in Eq. (5), clear evidence is provided that the dominant in-plane orbital is different for the two spin-split valence bands; in other words the radial-tangential *orbital texture switches* at $k = 0$, i.e., the band crossing point K^*. The model also reveals that the symmetry lowering away from K^* permits the mixing of new $m_j = \pm 3/2$ ($|+\rangle \otimes |\uparrow\rangle$ and $|-\rangle \otimes |\downarrow\rangle$, or "heavy hole"-like) components into the K^* wave functions ($m_j = \pm 1/2$ for the VB1 and VB2 of BiTeI), leading to the orbital texture switch.

Benefiting from the truncated basis set represented in terms of m_j, as distilled from the all-orbital DFT representation, we conclude that the underlying physical origin of the common behavior in both TI and non-TI materials is the SOC symmetry-enforced hybridization of different azimuthal total OAM m_j components into band eigenstates. This hybridization was absent at the high-symmetry K^* point. Thus this effect is not limited to topological insulators but is far more general and applies also to Rashba compounds that are topological-trivial bulk semiconductors such as BiTeI [34]. It is noticeable that the orbital switch is generally a small k effect available only in the vicinity of K^*, where p_x and p_y orbitals have equal intensity. Comparing with TI surface states, the Hamiltonian of BiTeI has an additional kinetic term $\hbar^2k^2/2m^*$, leading to two paraboliclike branches with a critical band crossing point. Unlike the TI Dirac cone, the band crossing point in a Rashba semiconductor seems trivial, but it still manifests such orbital texture switch, indicating the physical origin from the fundamental spin-orbital effects rather than the topological feature.

From Eq. (5) we can see that the orbital switch for both TI surface and Rashba bulk must occur at a critical point (Dirac point in TI and band crossing point in Rashba semiconductor) because of the symmetric form of the wave functions. However, the question of which orbital dominates a certain state depends on the wave-function coefficients, which is *material dependent*. Therefore, if the sample is inverted within a fixed laboratory frame (like the bottom surface of TI), the orbital texture will remain unchanged. On the other hand, the chirality of the spin texture of the Rashba system is *coordinate dependent*. The helical spin texture will change the chirality by the inversion of the sample, due to the flip of the polar field inside the crystal. This is analogous to the top and bottom surface states of Bi_2Se_3 in which the spin texture is opposite but the orbital texture has the same switching trend. We can also expect the truncated spin polarization and uncompensated spin polarization at the same k point for upper and lower Dirac cones [24,35–38] from the discussion mentioned above.

VI. UNDERSTANDING THE SPIN-POLARIZATION EFFECTS

Equations (3) and (4) show that each orbital component couples with a certain spin state, forming *orbital-dependent spin textures* [see Eq. (2)]. Maximal spin magnitude arises when every orbital-dependent spin texture coaligns, i.e., has the same helicity. This requires that the band eigenstate be composed exclusively of orbitals with the same azimuthal quantum number m_l. In real materials where SOC mixes orbitals with different m_l in one eigenstate (n, $\boldsymbol{k}$), the corresponding spin polarization is truncated relative to its maximal value. Specifically, the tangential in-plane orbital (p_t) always couples opposite spin texture to that of radial in-plane orbital (p_r), s, and p_z orbital. At the wave vector K^* with $k \to 0$, p_t and p_r components have the same intensity but opposite spin pattern and thus cancel each other, making the spin polarization $S(k \to 0) = |\omega_{\mathrm{VB}}|^2$ all contributed by the s and p_z orbitals. This scenario gives the truncated spin polarization at K^* for all the bands shown in Fig. 1(c). The total spin polarization summing over all bands is equivalent to the value obtained from the contributions of $m_l = 0$ states, e.g., s, p_z, and d_z^2, etc. This statement is valid also in the traditional 2D Rashba systems such as Au(111) surface [11], in which the surface Rashba bands are nearly exclusively composed by the s and p_z states, and thus have nearly 100% spin polarization.

Due to the orbital texture switch, we find from Eqs. (3) and (4) that the dominate in-plane p orbitals of a pair of Rashba bands couple to spin textures with the same helicity. This fact is confirmed by DFT calculation showing that the dominating radial orbital for VB1 and tangential orbital for VB2 both have RH spin texture (see Fig. 4). In BiTeI, the wave functions of VB1 and VB2 are dominated by $s + p_z$ orbitals [Te-p_z(∼50%),I − p_z(∼13%), and Bi-s (13%)]. We consider here two categories of orbitals classified by $m_l = 0$ (s and p_z for all sites) and $m_l \neq 0$ (in-plane p_x and p_y for all sites) and examine the corresponding spin textures coupled by these two classes. The $s + p_z$-dependent spin texture has opposite helicity for VB1 and VB2; i.e., VB1 has a right-handed (RH) spin texture, while VB2 has a left-handed (LH) spin texture (see Fig. 5). On the other hand, the in-plane orbital ($p_x + p_y$) also contributes helical spin textures, but these orbital-dependent spin textures have the same RH helicity for both VB1 and VB2, as shown by the white arrows in Figs. 4(a) and 4(b). This can also be understood by multiorbital model equations (1) and (2), where the $p_r(p_t)$ orbitals always provide positive (negative) contributions to the $s + p_z$-orbital-dependent spin textures. Consequently, at a finite k the different intensity of p_t and p_r orbitals for VB1 and VB2 can cause different spin magnitudes to the respective bands, and thus a nonzero net spin polarization $S_1(k) + S_2(k)$. From Fig. 4(a) we find that for VB1 p_r dominates the in-plane orbital, so the in-plane spin texture followed the radial feature, i.e., RH. On the other hand, for VB2 p_t dominates the in-plane orbital as shown in Fig. 4(b), so the total in-plane spin texture is still RH. Therefore, by summing the in-plane orbital contribution and the $s + p_z$ orbital contribution to the spin textures, the total spin polarization shows different spin truncation for VB1 and VB2, as shown in Fig. 1(c).

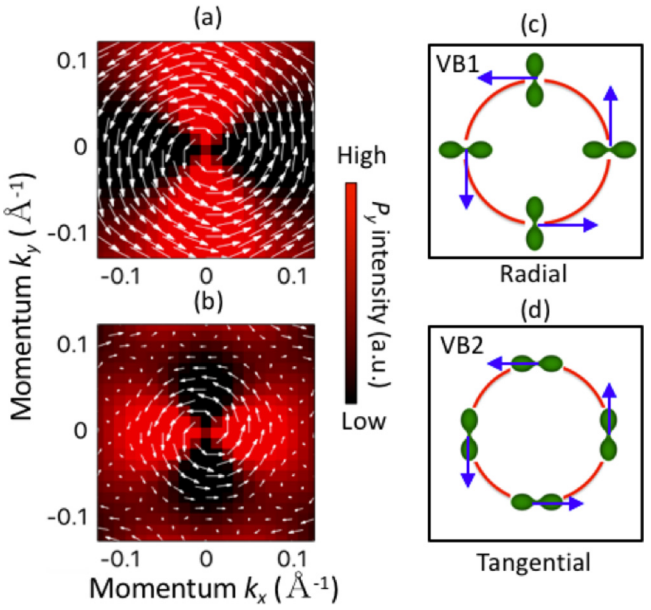

FIG. 4. (a,b) The in-plane p-dependent spin textures (white arrows) for VB1 (a) and VB2 (b). The background color indicates the p_y intensity. (c,d) Schematic plots for the radial orbital texture and the corresponding orbital-dependent spin texture of VB1 (c) and the tangential orbital texture and the corresponding orbital-dependent spin texture of VB2 (d).

Similar to VB1 and VB2, the degenerate state at A in CB1 and CB2 are also $m_j = \pm 1/2$ states. Therefore, they have the form of wave functions analogous to Eqs. (3) and (4), but with different wave-function coefficients. DFT shows that the weight of the $s + p_z$ orbital and in-plane p orbital is about 50%:50% at A [Bi-p_z(∼35%),Te-$p_{x,y}$(∼27%), and Bi-$p_{x,y}$ (18%)], leading to ±0.5 spin polarization. The spin textures as well as the $p_{x,y}$ and $s + p_z$ orbital-dependent spin textures for CB1 and CB2 are shown in Fig. 6. We find that the total spin texture is predominately contributed by the p_z orbital, while the $p_{x,y}$ orbital-dependent spin texture is negligible. This is because of the competition between the $p_{x,y}$ orbital textures of the Bi and Te atoms. Recalling that the tangential and radial orbitals always couple opposite spin textures [see Eqs. (3) and (4)], the similar distribution of the two kinds of orbitals in each conduction band leads to a canceling of in-plane orbital-dependent spin texture (see Fig. 3). In contrast, VB1 and VB2 have fewer $p_{x,y}$ components and are mainly from a single source (Te atom), so they manifest a larger spin magnitude and noncompensation effect by the same helicity of the in-plane orbital-dependent spin textures.

For VB3 and VB4, p_t and p_r dominate the whole state around K^*, respectively. Therefore, VB3 and VB4 bands are $m_j = \pm 3/2$ states with the corresponding wave functions at K^* containing only in-plane p components: $|+\rangle \otimes |\uparrow\rangle$ and $|-\rangle \otimes |\downarrow\rangle$, leading to the complete quenching of spin. Consequently, the total spin textures form two LH helical spin loops (see Fig. 3). Unlike the case in Bi/Cu(111) [13] and Bi/Ag(111) [15] surface alloys, these identical spin-rotating loops occur at the occupied bands that are detectable by ARPES measurements.

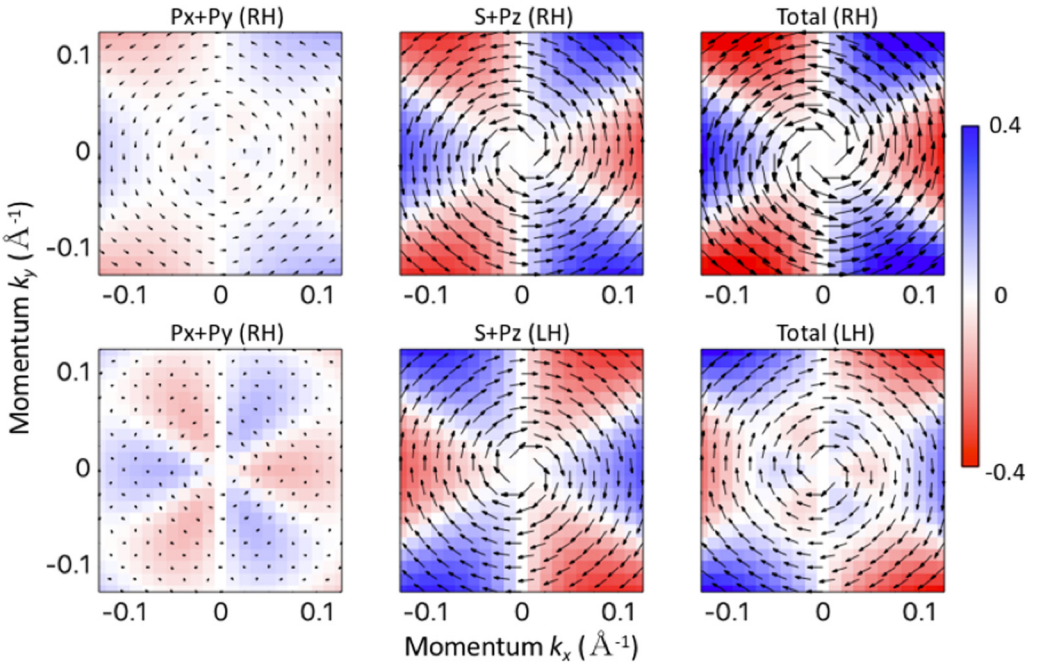

FIG. 5. Orbital-dependent spin texture coupled by in-plane p orbital ($p_x + p_y$) and $m_l = 0$ orbital ($s + p_z$), and the total spin texture of VB1 (upper row) and VB2 (lower row). The background color indicates the out-of-plane spin component S_z. LH (RH) denotes left-handed (right-handed) in-plane spin texture (S_x,S_y).

VII. EFFECTS OF DIFFERENT SOC STRENGTH

To demonstrate that the intriguing spin-polarization effects originate from SOC we artificially rescaled the strength of SOC by adding a multiplier Δ on the SOC Hamiltonian ($\Delta = 1$ for the real system). The spin magnitude and spin-splitting energy E_R for VB1 and VB2 of BiTeI as a function of Δ are shown in Fig. 7. Using a small SOC strength $\Delta = 0.01$ and extrapolating the results to $\Delta = 0$, we find that the two valence bands are degenerated with a fully polarized spin-up

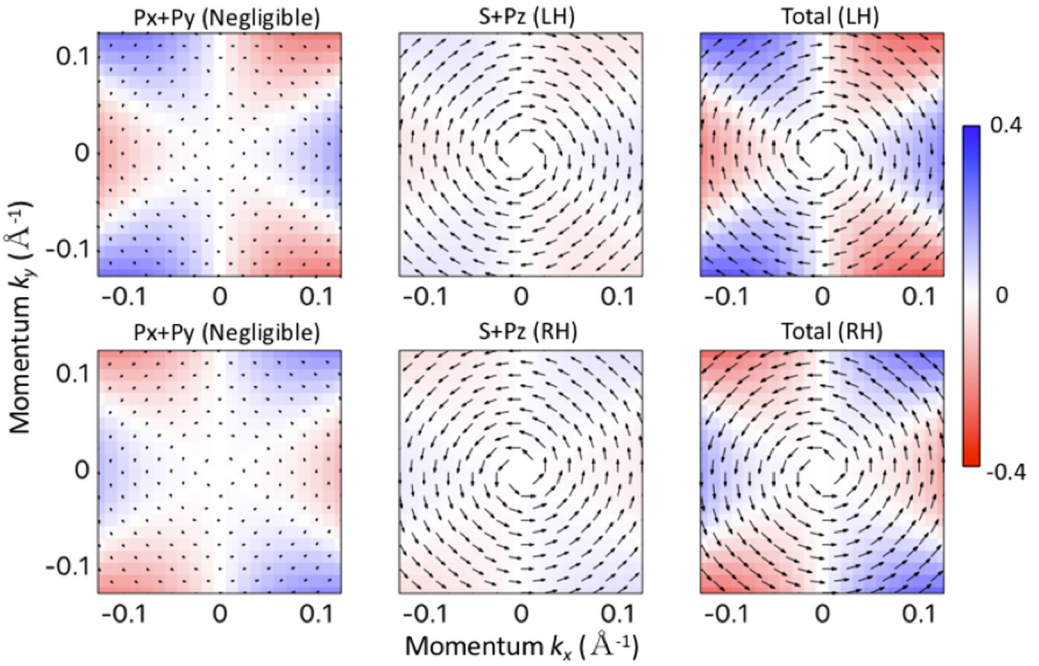

FIG. 6. Orbital-dependent spin texture coupled by in-plane p orbital ($p_x + p_y$) and $m_l = 0$ orbital ($s + p_z$), and the total spin texture of CB1 (lower row) and CB2 (upper row). The background color indicates the out-of-plane spin component S_z. LH (RH) denotes left-handed (right-handed) in-plane spin texture (S_x, S_y).

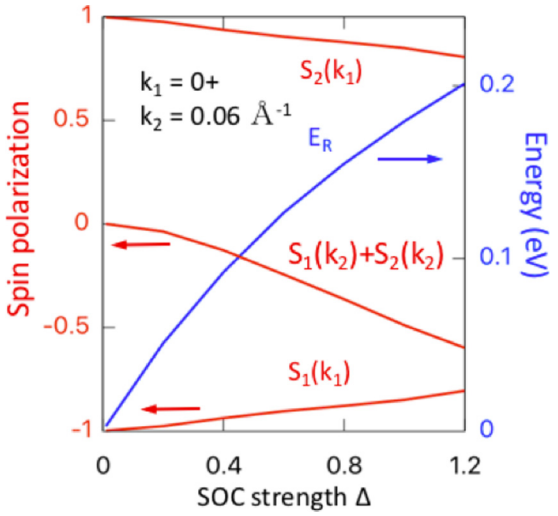

FIG. 7. Spin magnitude $S_1(k_1)$ at $k_1 = 0+$, $S_1(k_2) + S_1(k_2)$ at $k_2 = 0.06\,\text{Å}^{-1}$ along the k_y direction for VB1and VB2, and the spin-splitting energy E_R as a function of the strength of SOC.

and spin-down component [$S_1(k_1) = -1$ and $S_2(k_1) = 1$] with the absence of SOC. At this time the A states are composed by pure $m_l = 0$ orbitals, i.e., s and p_z. When increasing Δ, there is a reduction on spin magnitude at $k_1 \to 0$, i.e., the A point, due to the mixture of in-plane p orbitals. On the other hand, the spin polarizations of VB1 and VB2 apparently compensate for each other at A with $S_1(k_1) + S_2(k_1) = 0$, while away from the A point such as $k_2 = 0.06\,\text{Å}^{-1}$, the sum of spin magnitude of the valence bands deviates from zero with the increasing Δ. Therefore, it clearly shows that SOC not only manifests an energy splitting between spin-polarized bands, but also introduces a complex interplay between spin and multiorbitals leading to various spin-polarizations effects.

VIII. GENERALIZING TO SYSTEMS WITH INVERSION SYMMETRY

The truncated spin polarization and the net polarization effect are illustrated above in a Rashba semiconductor BiTeI. However, we are not using any special feature of this orbitally hybridized compound other than SOC-induced (Rashba) spin splitting, and thus expect our finding to pertain to a very broad range of such compounds, whether inversion symmetry is present or not. In centrosymmetric crystals the spin bands are degenerate in E vs k momentum space, but this does not mean that the spins are mixed in position space. Correspondingly, the centrosymmetric systems with lower-symmetry sectors could manifest a "hidden" form of spin polarization named the R-2 effect [25,39]. Like two oppositely stacked Rashba layers, in the R-2 system there is still finite spin polarization localized on each atomic site i that feels in a locally inversion-asymmetric environment, leading to polarization that is compensated in k space by another atom forming an inversion partner of site i. Therefore, if we consider the local spin polarization in real space, i.e., localized on one inversion-asymmetric atom or sector, the spin-truncation effects also happen when spin is coupled by multiorbitals with different m_l. It is noticeable that the orbital-dependent spin texture is robust against the situation when a small perturbation breaks the global inversion symmetry, such as electric fields. This is highly feasible for the detection in experiments.

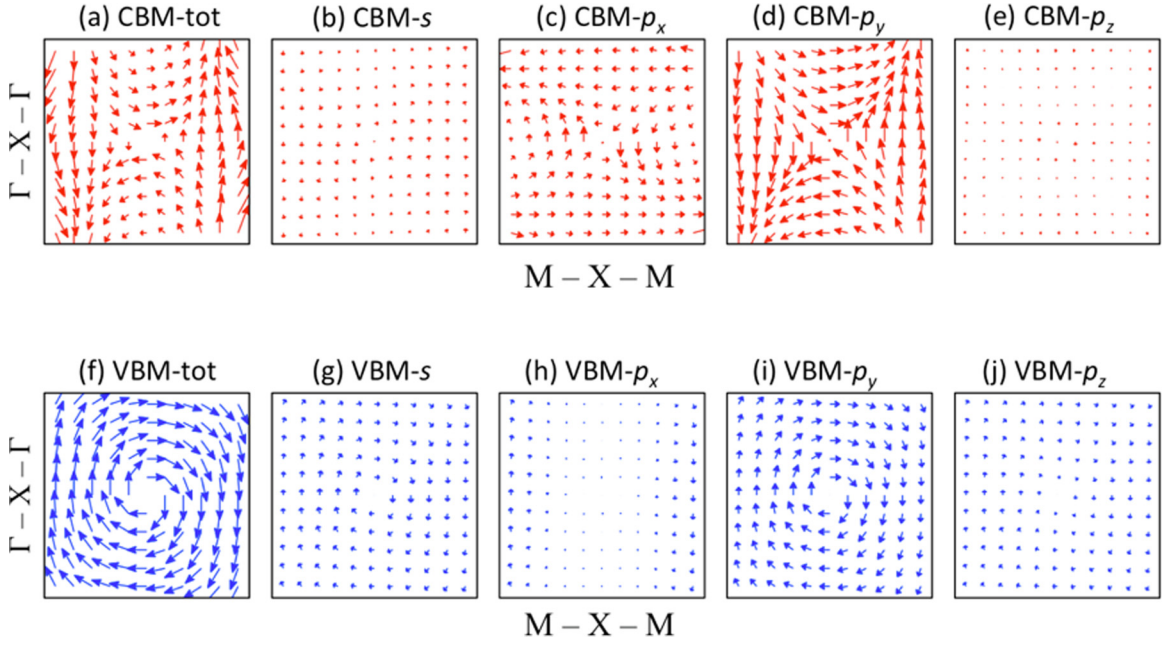

FIG. 8. (a) Local spin texture of $LaOBiS_2$ projected on one BiS_2 layer for CBM. (b–e) Local spin texture for CBM contributed from s, p_x, p_y, and p_z atomic orbitals, respectively. (e) Same as (a), but for VBM. (f–j) Same as (b–e), but for VBM. For clarity, the arrow scale of (a–e) is twice as that of (e–h).

TABLE I. Direction of atomic-orbital-dependent spin textures in the vicinity of the X point. S_1 and S_2 form in-plane and perpendicular Bi-S bonds, respectively.

	s	p_x	p_y	p_z
Bi	+	+	−	+
S_1	−	−	+	−
S_2	+	+	−	+

We choose a centrosymmetric R-2 material, $LaOBiS_2$ (using the reported space group $P4/nmm$), to illustrate the truncation effects. Figures 8(a) and 8(e) exhibit the projected atomic-orbital-dependent spin textures of $LaOBiS_2$ on one BiS_2 layer of the twofold degenerated conduction band minimum (CBM) and valence band maximum (VBM), respectively. The local spin textures on the other BiS_2 layer are exactly oppositely formed [25], and are not shown here. All the spin textures are in the x-y plane, with almost zero z component. We observe helical spin for holes but nonhelical spin for electrons, suggesting Rashba-type polarization (R-2) and the combination of Rashba and Dresselhaus effects (R-2 and D-2) for VBM and CBM, respectively. In general, the environment of R-2 material contains simultaneously polar field and inversion asymmetry, indicating the coexistence of R-2 and D-2 effects, depending on different band characters.

We note that the hole spin is nearly fully polarized with the spin magnitude ∼90%, while the electron spin is only ∼30% polarized. Besides the spin mixture effect due to the interlayer coupling (vanished along the X-M direction), the reason that leads to the partial polarization is the diverse atomic-orbital-dependent spin textures. Figures 8(b)–8(d) and 8(f)–8(h) show the spin textures from different atomic orbitals within one BiS_2 layer. We see all the orbital-dependent spin textures are parallel or antiparallel to the total spin texture, and they can make either positive or negative effects on the total spin polarization. We consider four atomic orbitals s, p_x, p_y, and p_z for each site of one BiS_2 layer. Table I shows the sign of spin polarization induced by each atomic orbital of different sites, valid for both VB and CB. The whole expectation of the local spin is calculated by adding all the 12 orbital-projected components. Looking into different orbitals, we find that for each site, s, p_x, and p_z have the same spin direction, while p_y always has the opposite one, which is determined by the band symmetry character around the X point. At the X (0, 1/2, 0) point, the nonequivalence between x and y direction leads to anisotropic feature between p_x and p_y. The VBM is mainly composed of Bi-s and S-p_y states, with the same spin helicity (2 "+"). On the other hand, the CBM is dominated by Bi-p_x and p_y states, which couple antiparallel spin textures (1 "+" and 1 "–"). Therefore, the total spin polarization of electrons is strongly reduced compared with the holes.

IX. DISCUSSION AND DESIGN IMPLICATIONS

In the past few years wide areas of physics and material science that related to SOC have built up the new field of spin orbitronics. By generalizing the previously observed orbital texture switch in TI surface to a bulk Rashba semiconductor, we unveil the deeper mechanism of various spin-polarization effects that are unexpected in the simple Rashba model, and provide a clear picture of the delicate interplay between spin and multiorbitals. Our work, particularly the atomic-orbital feature, is also expected to open a route for designing high-spin-polarization materials that are of vital importance for nonmagnetic spintronic applications [3]. For example, in Rashba splitting the in-plane spin drives a current perpendicular to the direction of spin polarization induced by the asymmetric Elliot-Yafet spin relaxation, named the spin-galvanic effect [26,27]. Since the current is proportional to the average magnitude of the spin polarization, the effects of spin truncation and the fact that different branches experience different degrees of spin polarization could have a more complex impact on the conversion process between spin and current in a Rashba system, which calls for further investigation.

ACKNOWLEDGMENTS

We are grateful for helpful discussions with Dr. Yue Cao. This work was supported by NSF Grant No. DMREF-13-34170. This work used the Extreme Science and Engineering Discovery Environment (XSEDE), which is supported by National Science Foundation Grant No. ACI-1053575.

APPENDIX: $k \cdot p$ WAVE FUNCTIONS OF MULTIBAND RASHBA MODEL

The model starts from the basic spin doublets at the band crossing K^* point and expands the wave functions to a small wave vector $\boldsymbol{k}$ away from K^* [Eqs. (3) and (4) of the main text], to see how different p orbitals couple the spin angular momentum with a LH or RH texture. Without the loss of generality, we consider the K^* state with the azimuth total angular momentum m_j being $\pm\frac{1}{2}$, as the case of VB1 and VB2 in BiTeI (double group representation A_4). We can therefore write the doubly degenerate states at the A point as [33,40]

$$\left|A_{4v},\tfrac{1}{2}\right\rangle = \sqrt{1-\omega_{\mathrm{VB}}^2}|+\rangle\otimes|\downarrow\rangle + \omega_{\mathrm{VB}}|Z\rangle\otimes|\uparrow\rangle, \quad \text{(A1)}$$

$$\left|A_{4v},-\tfrac{1}{2}\right\rangle = \sqrt{1-\omega_{\mathrm{VB}}^2}|-\rangle\otimes|\uparrow\rangle + \omega_{\mathrm{VB}}|Z\rangle\otimes|\downarrow\rangle, \quad \text{(A2)}$$

where ω_{VB} is the wave-function coefficient that can be determined by DFT calculation. $|Z\rangle = \omega_s|s\rangle + \omega_z|p_z\rangle$ where $|\omega_s|^2 + |\omega_z|^2 = 1$ and $|\pm\rangle = \mp(|p_x\rangle \pm i|p_y\rangle)/\sqrt{2}$ stand for different orbital basis. The $|+\rangle$, $|-\rangle$, and $|Z\rangle$ bases hold the orbital angular momentum $m_l = 1, -1$, and 0, respectively, coupling with certain spin angular momenta to preserve the total angular momentum m_j. Although the spin splitting happens at the wave vectors away from A, the zero-order wave functions at A still need to approximately fit the Rashba Hamiltonian $H_R = \alpha(\sigma_y k_x - \sigma_x k_y)$, written as the matrix form in the following:

$$H_R = \alpha|k|\begin{pmatrix} 0 & -ie^{-i\theta} \\ ie^{i\theta} & 0 \end{pmatrix}. \quad \text{(A3)}$$

Therefore, the zero-order wave functions at A are written as

$$|\mathrm{VB1},0+\rangle = \frac{1}{\sqrt{2}}\left[-ie^{-i\theta}\left|A_{4v},\frac{1}{2}\right\rangle + \left|A_{4v},-\frac{1}{2}\right\rangle\right]$$
$$= \frac{1}{\sqrt{2}}\left[\sqrt{1-\omega_{\mathrm{VB}}^2}|-\rangle - ie^{-i\theta}\omega_{\mathrm{VB}}|Z\rangle\right]\otimes|\uparrow\rangle - \left[\frac{1}{\sqrt{2}}ie^{-i\theta}\sqrt{1-\omega_{\mathrm{VB}}^2}|+\rangle - \omega_{\mathrm{VB}}|Z\rangle\right]\otimes|\downarrow\rangle, \tag{A4}$$

$$|\mathrm{VB1},0-\rangle = \frac{1}{\sqrt{2}}\left[-ie^{-i\theta}\left|A_{4v},\frac{1}{2}\right\rangle + \left|A_{4v},-\frac{1}{2}\right\rangle\right]$$
$$= \frac{1}{\sqrt{2}}\left[\sqrt{1-\omega_{\mathrm{VB}}^2}|-\rangle + ie^{-i\theta}\omega_{\mathrm{VB}}|Z\rangle\right]\otimes|\uparrow\rangle + \left[\frac{1}{\sqrt{2}}ie^{-i\theta}\sqrt{1-\omega_{\mathrm{VB}}^2}|+\rangle + \omega_{\mathrm{VB}}|Z\rangle\right]\otimes|\downarrow\rangle. \tag{A5}$$

Using the rotational in-plane coordinate system with tangential, radial direction to present the quantum number states $|+\rangle$ and $|-\rangle$, we have

$$\begin{pmatrix}|+\rangle\\|-\rangle\end{pmatrix} = \frac{1}{\sqrt{2}}\begin{pmatrix}-1 & -i\\ 1 & -i\end{pmatrix}\begin{pmatrix}|p_x\rangle\\|p_y\rangle\end{pmatrix} = \frac{1}{\sqrt{2}}\begin{pmatrix}-ie^{i\theta} & -e^{i\theta}\\ -ie^{-i\theta} & e^{-i\theta}\end{pmatrix}\begin{pmatrix}p_t\\p_r\end{pmatrix}. \tag{A6}$$

For the spin part, we use the $|\mathrm{LH}\rangle$ and $|\mathrm{RH}\rangle$ helical spin states to present $|\uparrow\rangle$ and $|\downarrow\rangle$:

$$\begin{pmatrix}|\uparrow\rangle\\|\downarrow\rangle\end{pmatrix} = \frac{1}{\sqrt{2}}\begin{pmatrix}-ie^{i\theta} & ie^{i\theta}\\ 1 & 1\end{pmatrix}\begin{pmatrix}|\mathrm{LH}\rangle\\|\mathrm{RH}\rangle\end{pmatrix}. \tag{A7}$$

Then we can rewrite Eqs. (A6) and (A7) as

$$|\mathrm{VB1},0+\rangle = \frac{1}{\sqrt{2}}\sqrt{1-\omega_{\mathrm{VB}}^2}|p_t\rangle\otimes|\mathrm{LH}\rangle + \left[-\frac{i}{\sqrt{2}}\sqrt{1-\omega_{\mathrm{VB}}^2}|p_r\rangle + \omega_{\mathrm{VB}}|Z\rangle\right]\otimes|\mathrm{RH}\rangle, \tag{A8}$$

$$|\mathrm{VB2},0+\rangle = -\frac{1}{\sqrt{2}}\sqrt{1-\omega_{\mathrm{VB}}^2}|p_t\rangle|\mathrm{RH}\rangle + \left[\frac{i}{\sqrt{2}}\sqrt{1-\omega_{\mathrm{VB}}^2}|p_r\rangle + \omega_{\mathrm{VB}}|Z\rangle\right]\otimes|\mathrm{LH}\rangle. \tag{A9}$$

These are the zero-order wave functions of A states with the azimuth total angular momentum $m_j = \frac{1}{2}$. Equations (A8) and (A9) already reveal many observations found by our DFT calculation in the main text. For example, the tangential orbital always couples opposite spin textures with the radial orbital and s and p_z orbitals. Furthermore, at the A point the tangential and radial orbitals have the same intensity but opposite spin textures canceling each other. Therefore, the spin magnitude at the A point is determined by the intensity of the s and p_z orbitals.

The first-order wave functions at the A point involve the linear k term, which can be presented using $k_\pm$ that have fixed $m_l = \pm 1$, written as

$$\left|A_{4v},-\tfrac{1}{2}\right\rangle^{(1)} = -a_{\mathrm{VB}}k_+|Z\rangle\otimes|\downarrow\rangle - b_{\mathrm{VB}}k_+|-\rangle\otimes|\uparrow\rangle + c_{\mathrm{VB}}k_-|+\rangle\otimes|\uparrow\rangle, \tag{A10}$$

$$\left|A_{4v},-\tfrac{1}{2}\right\rangle^{(1)} = -a_{\mathrm{VB}}k_-|Z\rangle\otimes|\uparrow\rangle - b_{\mathrm{VB}}k_-|+\rangle\otimes|\downarrow\rangle - c_{\mathrm{VB}}k_+|-\rangle\otimes|\downarrow\rangle, \tag{A11}$$

where $k_\pm = k_x \pm ik_y$, and a_{VB}, b_{VB}, c_{VB} are wave-function coefficients. Note that we have used the conservation of the total angular momentum along the z direction to construct the wave functions by involving the angular momentum of $k_\pm$ as ± 1, while $|+\rangle\otimes|\uparrow\rangle$ and $|-\rangle\otimes|\downarrow\rangle$ themselves are "heavy hole"-like components with $m_j = \pm 3/2$. Similarly, considering the Rashba Hamiltonian the first-order wave functions of the valence bands are written as

$$|\mathrm{VB1},k\rangle^{(1)} = \frac{1}{\sqrt{2}}\left[-ie^{-i\theta}\left|A_{4v},\frac{1}{2}\right\rangle + \left|A_{4v},-\frac{1}{2}\right\rangle\right]$$
$$= \frac{i}{\sqrt{2}}(b_{\mathrm{VB}}+c_{\mathrm{VB}})k|p_t\rangle\otimes|\mathrm{LH}\rangle + \left[\frac{1}{\sqrt{2}}(b_{\mathrm{VB}}-c_{\mathrm{VB}})k|p_r\rangle - ia_{\mathrm{VB}}k|Z\rangle\right]\otimes|\mathrm{RH}\rangle, \tag{A12}$$

$$|\mathrm{VB2},k\rangle^{(1)} = \frac{1}{\sqrt{2}}\left[ie^{-i\theta}\left|A_{4v},\frac{1}{2}\right\rangle + \left|A_{4v},-\frac{1}{2}\right\rangle\right]$$
$$= \frac{i}{\sqrt{2}}(b_{\mathrm{VB}}+c_{\mathrm{VB}})k|p_t\rangle\otimes|\mathrm{RH}\rangle + \left[\frac{1}{\sqrt{2}}(b_{\mathrm{VB}}-c_{\mathrm{VB}})k|p_r\rangle + ia_{\mathrm{VB}}k|Z\rangle\right]\otimes|\mathrm{LH}\rangle. \tag{A13}$$

Considering $\mu_{\mathrm{VB}} = i(b_{\mathrm{VB}}+c_{\mathrm{VB}})$, $v_{\mathrm{VB}} = b_{\mathrm{VB}}-c_{\mathrm{VB}}$, and $\xi_{\mathrm{VB}} = ia_{\mathrm{VB}}$ and combining zero-order and first-order wave functions equations (A8), (A9), (A12), and (A13) together we obtain the exact form of Eqs. (3) and (4). In addition, only if $c_{\mathrm{VB}} = 0$, i.e., the $|+\rangle\otimes|\uparrow\rangle$ and $|-\rangle\otimes|\downarrow\rangle$ components in Eqs. (A10) and (A11) are absent, would the orbital switching be avoided. Therefore, the origin of the orbital texture switch is attributed to the mixing of $m_j = \pm 3/2$ states.

[1] A. Manchon, H. C. Koo, J. Nitta, S. M. Frolov, and R. A. Duine, Nat. Mater. **14**, 871 (2015).

[2] C. Ciccarelli, M. D. HalsKjetil, A. Irvine, V. Novak, Y. Tserkovnyak, H. Kurebayashi, A. Brataas, and A. Ferguson, Nat. Nanotechnol. **10**, 50 (2015).

[3] I. Žutić, J. Fabian, and S. Das Sarma, Rev. Mod. Phys. **76**, 323 (2004).

[4] G. Dresselhaus, Phys. Rev. **100**, 580 (1955).

[5] Y. A. Bychkov and E. I. Rashba, JETP Lett. **39**, 78 (1984).

[6] A. Manchon, Nat. Phys. **10**, 340 (2014).

[7] H. Kurebayashi, J. Sinova, D. Fang, A. C. Irvine, T. D. Skinner, J. Wunderlich, V. Novak, R. P. Campion, B. L. Gallagher, E. K. Vehstedt, L. P. Zarbo, K. Vyborny, A. J. Ferguson, and T. Jungwirth, Nat. Nanotechnol. **9**, 211 (2014).

[8] M. Z. Hasan and C. L. Kane, Rev. Mod. Phys. **82**, 3045 (2010).

[9] V. Mourik, K. Zuo, S. M. Frolov, S. R. Plissard, E. P. A. M. Bakkers, and L. P. Kouwenhoven, Science **336**, 1003 (2012).

[10] A. Koga, N. Kawakami, T. M. Rice, and M. Sigrist, Phys. Rev. Lett. **92**, 216402 (2004).

[11] J. Henk, A. Ernst, and P. Bruno, Phys. Rev. B **68**, 165416 (2003).

[12] G. Bihlmayer, S. Blügel, and E. V. Chulkov, Phys. Rev. B **75**, 195414 (2007).

[13] H. Mirhosseini, J. Henk, A. Ernst, S. Ostanin, C.-T. Chiang, P. Yu, A. Winkelmann, and J. Kirschner, Phys. Rev. B **79**, 245428 (2009).

[14] H. Hirayama, Y. Aoki, and C. Kato, Phys. Rev. Lett. **107**, 027204 (2011).

[15] S. N. P. Wissing, A. B. Schmidt, H. Mirhosseini, J. Henk, C. R. Ast, and M. Donath, Phys. Rev. Lett. **113**, 116402 (2014).

[16] E. E. Krasovskii, J. Phys.: Condens. Matter **27**, 493001 (2015).

[17] S. Schirone, E. E. Krasovskii, G. Bihlmayer, R. Piquerel, P. Gambardella, and A. Mugarza, Phys. Rev. Lett. **114**, 166801 (2015).

[18] M. S. Bahramy, P. D. C. King, A. de la Torre, J. Chang, M. Shi, L. Patthey, G. Balakrishnan, P. Hofmann, R. Arita, N. Nagaosa, and F. Baumberger, Nat. Commun. **3**, 1159 (2012).

[19] I. Zeljkovic, Y. Okada, C.-Y. Huang, R. Sankar, D. Walkup, W. Zhou, M. Serbyn, F. Chou, W.-F. Tsai, H. Lin, A. Bansil, L. Fu, M. Z. Hasan, and V. Madhavan, Nat. Phys. **10**, 572 (2014).

[20] Z. Xie, S. He, C. Chen, Y. Feng, H. Yi, A. Liang, L. Zhao, D. Mou, J. He, Y. Peng, X. Liu, Y. Liu, G. Liu, X. Dong, L. Yu, J. Zhang, S. Zhang, Z. Wang, F. Zhang, F. Yang *et al.*, Nat. Commun. **5**, 3382 (2014).

[21] Z. Zhiyong, C. Yingchun, and S. Udo, New J. Phys. **15**, 023010 (2013).

[22] H. Zhang, C.-X. Liu, and S.-C. Zhang, Phys. Rev. Lett. **111**, 066801 (2013).

[23] Y. Cao, J. A. Waugh, X. W. Zhang, J. W. Luo, Q. Wang, T. J. Reber, S. K. Mo, Z. Xu, A. Yang, J. Schneeloch, G. D. Gu, M. Brahlek, N. Bansal, S. Oh, A. Zunger, and D. S. Dessau, Nat. Phys. **9**, 499 (2013).

[24] Z. H. Zhu, C. N. Veenstra, G. Levy, A. Ubaldini, P. Syers, N. P. Butch, J. Paglione, M. W. Haverkort, I. S. Elfimov, and A. Damascelli, Phys. Rev. Lett. **110**, 216401 (2013).

[25] X. Zhang, Q. Liu, J.-W. Luo, A. J. Freeman, and A. Zunger, Nat. Phys. **10**, 387 (2014).

[26] S. D. Ganichev, P. Schneider, V. V. Bel'kov, E. L. Ivchenko, S. A. Tarasenko, W. Wegscheider, D. Weiss, D. Schuh, B. N. Murdin, P. J. Phillips, C. R. Pidgeon, D. G. Clarke, M. Merrick, P. Murzyn, E. V. Beregulin, and W. Prettl, Phys. Rev. B **68**, 081302 (2003).

[27] S. D. Ganichev, E. L. Ivchenko, V. V. Bel'kov, S. A. Tarasenko, M. Sollinger, D. Weiss, W. Wegscheider, and W. Prettl, Nature **417**, 153 (2002).

[28] K. Ishizaka, M. S. Bahramy, H. Murakawa, M. Sakano, T. Shimojima, T. Sonobe, K. Koizumi, S. Shin, H. Miyahara, A. Kimura, K. Miyamoto, T. Okuda, H. Namatame, M. Taniguchi, R. Arita, N. Nagaosa, K. Kobayashi, Y. Murakami, R. Kumai, Y. Kaneko *et al.*, Nat. Mater. **10**, 521 (2011).

[29] G. Kresse and D. Joubert, Phys. Rev. B **59**, 1758 (1999).

[30] J. P. Perdew, K. Burke, and M. Ernzerhof, Phys. Rev. Lett. **77**, 3865 (1996).

[31] P. Błoński and J. Hafner, Phys. Rev. B **79**, 224418 (2009).

[32] G. Kresse and J. Furthmüller, Comput. Mater. Sci. **6**, 15 (1996).

[33] M. S. Bahramy, R. Arita, and N. Nagaosa, Phys. Rev. B **84**, 041202 (2011).

[34] L. Bawden, J. M. Riley, C. H. Kim, R. Sankar, E. J. Monkman, D. E. Shai, H. I. Wei, E. B. Lochocki, J. W. Wells, W. Meevasana, T. K. Kim, M. Hoesch, Y. Ohtsubo, P. Le Fèvre, C. J. Fennie, K. M. Shen, F. Chou, and P. D. C. King, Sci. Adv. **1**, e1500495 (2015).

[35] D. Hsieh, Y. Xia, D. Qian, L. Wray, J. H. Dil, F. Meier, J. Osterwalder, L. Patthey, J. G. Checkelsky, N. P. Ong, A. V. Fedorov, H. Lin, A. Bansil, D. Grauer, Y. S. Hor, R. J. Cava, and M. Z. Hasan, Nature **460**, 1101 (2009).

[36] S. Souma, K. Kosaka, T. Sato, M. Komatsu, A. Takayama, T. Takahashi, M. Kriener, K. Segawa, and Y. Ando, Phys. Rev. Lett. **106**, 216803 (2011).

[37] S.-Y. Xu, Y. Xia, L. A. Wray, S. Jia, F. Meier, J. H. Dil, J. Osterwalder, B. Slomski, A. Bansil, H. Lin, R. J. Cava, and M. Z. Hasan, Science **332**, 560 (2011).

[38] M. Neupane, A. Richardella, J. Sánchez-Barriga, S. Xu, N. Alidoust, I. Belopolski, C. Liu, G. Bian, D. Zhang, D. Marchenko, A. Varykhalov, O. Rader, M. Leandersson, T. Balasubramanian, T.-R. Chang, H.-T. Jeng, S. Basak, H. Lin, A. Bansil, N. Samarth, and M. Z. Hasan, Nat. Commun. **5**, 3841 (2014).

[39] Q. Liu, X. Zhang, H. Jin, K. Lam, J. Im, A. J. Freeman, and A. Zunger, Phys. Rev. B **91**, 235204 (2015).

[40] L. C. Lew Yan Voon, M. Willatzen, M. Cardona, and N. E. Christensen, Phys. Rev. B **53**, 10703 (1996).